CHAPTER 6

Silver-loaded starch functionalized Fe_3O_4 photocatalyst for H_2O_2 production: Experimental and molecular dynamics studies

6.1 INTRODUCTION

A significant challenge for industrial applications of heterogeneous photocatalysts is their separation from the reaction system, recycling, and reuse [203]. Superparamagnetic photocatalysts can be separated by magnetic decantation. After separation, the external magnetic field is removed, and photocatalyst nanoparticles can be re-dispersed in a separate solution by simply stirring [29,204]. In this context, fine Fe_3O_4 nanoparticles are superparamagnetic, economical, and have visible range band gaps (1.9-2.4 eV) [205]. More importantly, the positions of its valence band (VB) and conduction band (CB) are well-aligned with the thermodynamic requirements for the two-electron ORR. Nevertheless, bare Fe_3O_4 nanoparticles suffer from poor water dispersibility. Fine Fe_3O_4 nanoparticles, stabilized by various organic modifiers such as dextrin and citrate, exhibit band gaps exceeding 2.1 eV due to quantum size effects and enhanced water dispersibility [59,206]. Similarly, starch-stabilized magnetite nanoparticles display a comparable band gap and demonstrate excellent water dispersibility. Starch emerges as one of the potential functionalization agents in magnetite synthesis because it is green, abundant, and cost-effective. Starch contains many O-H functional groups and can bind to the surface of the nanoparticles at the initial nucleation stage [59,207].

Adding a suitable noble metal cocatalyst (like Au, Ag, Pd, and Pt) to the primary semiconductor photocatalyst has been recommended to improve charge separation, O_2 adsorption, and its reduction [181,208,209]. For instance, H_2O_2 formation increases when co-catalysts like Ag or Au nanostructures are attached to the semiconductor part [36,41]. Moreover, the nanoparticles of these noble metals strongly absorb visible light of specific wavelengths owing to their localized surface plasmon resonance (LSPR) effect [65,86]. The re-emission of the absorbed energy in the visible range enhances the light absorption efficiency of the photocatalyst. The latter is an added advantage besides the cocatalyst

properties. Moreover, the relatively lower cost of Ag nanoparticles favors their use as cocatalysts. Thus, Tsukamoto and colleagues reported the enhanced photocatalytic production of H_2O_2 on the Ag/TiO_2 composite [41]. This improvement was attributed to the plasmonic Ag metal cocatalyst, generating photo-excited electrons with suitable redox potentials capable of effectively reducing oxygen [210].

The current study investigates the photocatalytic H_2O_2 production activity on Ag-loaded starch functionalized magnetite composite nanoparticles. Note that photocatalytic H_2O_2 production on this composite has not been reported previously. The optical properties and band edges of the composite nanoparticles are thoroughly investigated. Their H_2O_2 production photocatalytic activity is compared to pristine Fe_3O_4 nanoparticles and Ag-loaded Fe_3O_4 nanoparticles (without starch functionalization). Most photocatalysts reported in literature generate H_2O_2 from aqueous solutions of sacrificial agents, including methanol, ethanol, isopropanol, and oxalic acid [129,131]. Only a few photocatalysts have reported H_2O_2 production from pure water [49,211]. In this context, green and economical sacrificial agents can also be used. Glycerol is a byproduct of biodiesel production, green and economical, but very few publications have investigated its efficacy as a sacrificial agent [212]. The present chapter of this thesis also investigates and compares the photocatalytic H_2O_2 production effectiveness from aqueous solutions of different sacrificial agents mentioned above.

Photogenerated charge transfer and separation in Ag-loaded starch functionalized magnetite composite nanoparticles are examined using photoluminescence (PL) and electrochemical analysis. X-ray photoelectron spectroscopy (XPS) analyzed the chemical species and their oxidation states on the composite surface. Large-scale classical molecular dynamics (MD) simulations investigated the adsorption affinity of O_2 and H_2O molecules on the Fe_3O_4, starch functionalized Fe_3O_4, and Ag-loaded starch functionalized Fe_3O_4

composite systems. Several control experiments and MD simulations were conducted to obtain insight into the photocatalytic H_2O_2 production mechanism.

6.2 EXPERIMENTAL SECTION

6.2.1 Synthesis of starch-functionalized magnetite

A suitable volume of 0.4 M NaOH solution was heated at 80°C. Then, an aqueous solution of iron (II) sulfate heptahydrate ($FeSO_4.7H_2O$; 0.2M) and two wt.% starch was added dropwise to it from a burette. The temperature of the reaction mixture was maintained at 80°C throughout this process, and the reaction was continued for 2 hours until the complete formation of a black precipitate. This precipitate was separated by magnetic decantation and washed several times with distilled water and ethanol until the pH became neutral. Next, the washed precipitate was dried at 60°C for 24 hours. This Chapter uses the abbreviation 'SM' (starch-functionalized magnetite) for these nanoparticles. A sample of Fe_3O_4 nanoparticles, without starch, was also prepared using a similar synthesis protocol.

6.2.2 Synthesis of Ag-loaded SM

An appropriate amount of SM nanoparticles was dispersed in distilled water by bath sonication for 30 minutes. Next, a calculated amount of $AgNO_3$ (5,10, and 20 wt.%) solution was added to the dispersed solution of SM. The aqueous dispersion was agitated in a shaker for 12 hours. Then, 1 wt.% starch and 0.1 M glucose were added to the mixture and heated at 60°C for one hour. The pH of the mixture was maintained carefully at ~ 8 by adding an appropriate amount of 0.2M NaOH solution. Next, the prepared composite was separated magnetically, and the product was washed multiple times with distilled water (DW) and ethanol. The product was subsequently dried for 20 hours at 50°C. The resulting samples were coded as 'ASM' for Ag-loaded SM, with specific designations 5ASM,

10ASM, and 20ASM corresponding to the weight percentages (5%, 10%, and 20%) of $AgNO_3$ used during synthesis. Additionally, another sample with 10 wt% Ag loading on Fe_3O_4 nanoparticles was synthesized following a similar protocol, except without the addition of starch. This sample is labeled as 10AM, denoting 10 wt% Ag loaded on Fe_3O_4. The synthesis pathway for the ASM photocatalysts is illustrated in Scheme 6.1.

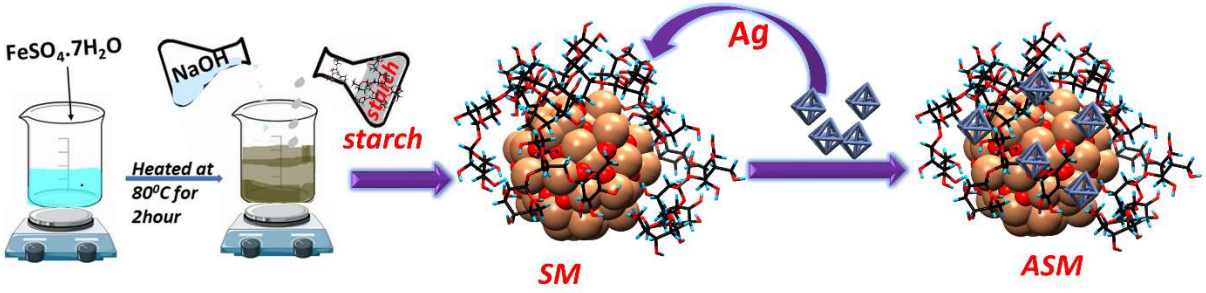

Scheme 6.1. The synthesis pathway of ASM photocatalysts.

6.2.3 Photocatalysis procedure

The photocatalyst sample (1 mg) was suspended in pure water or a sacrificial agent/water mixture (5/95%v/v; 12 mL) in a quartz tube. The tube was sealed with a silicone rubber septum cap. Bath sonication was conducted for 10 minutes to ensure proper catalyst dispersion in the reaction mixture. Oxygen was bubbled into the suspension. Subsequently, the mixture was kept in the dark for 60 minutes to reach adsorption-desorption equilibrium. After that, the above-prepared mixture was photo-irradiated with visible light (cool white LED source; 1070 W/m^2) for 60 minutes. The photocatalyst nanocomposite particles were quickly recovered from the suspension by magnetic separation. The H_2O_2 production in the remaining aqueous solution was monitored by an iodometric method. Separate photocatalytically produced H_2O_2 measurement experiments were performed under similar conditions with pure water, 5 vol% isopropanol, 5 vol% ethanol, and 5 vol% glycerol aqueous suspensions.

6.2.4 Computational studies

The Materials and Process Simulation software (MAPS 4.01 by Scienomics) was used to construct the molecular models for MD simulations. Three cases of the interaction of H_2O_2 with Fe_3O_4, SM, and ASM cluster models were simulated. An initial supercell model was built using an inverse spinel FCC unit cell of Fe_3O_4 (COD entry number: 907644). A nanocluster of 149 atoms (Fe69O80) was carved out from the Fe_3O_4 supercell. The diameter of this Fe_3O_4 nanocluster model is ~1.4 nm. This Fe_3O_4 nanocluster was then placed in the center of a cubic simulation box measuring 40 Å × 40 Å × 40 Å in dimensions (Figure 6.1a).

The first step for modeling SM was constructing an amylopectin (AMC) unit composed of the $C_{24}H_{41}O_{21}$ molecular formula using the molecular builder plugin in MAPS software. The amylopectin unit was optimized by Modified Neglect of Diatomic Overlap (MNDO) using MAPS software. Then, five amylopectin units were positioned close to the above-constructed Fe_3O_4 nanocluster (Figure 6.1b). After initial optimization, an MD equilibration run of ~1 ns was used to adsorb the amylopectin onto the magnetite nanocluster surface. The resulting model of the starch-functionalized Fe_3O_4 nanocluster is named 'SFC'. Similarly, the third model, Ag-loaded SM, was constructed. In the first step, a 0.6 nm Ag nanocluster with six atoms was cut out from an FCC Ag supercell. Subsequently, this Ag nanocluster was placed on the previously constructed SFC model (Figure 6.1c) and referred to as 'AgSFC'.

H_2O and O_2 molecules were constructed using the molecule builder plugin in MAPS and then optimized by the MNDO method. The H_2O molecules thus constructed and optimized were then modified with charges from the standard simple point charge (SPC) water model. The SPC charges for water molecules for hydrogen and oxygen are given in Table 6.1. This study inserted 20 O_2 and 2000 H_2O molecules into the Fe_3O_4, SM, and ASM

cubic cluster systems. The complete systems are hereafter called 'FC', 'SFC', and 'AgSFC' models, respectively. The O_2 and H_2O insertions maintained a fixed density of approximately 1.05 g/cc. Next, the conjugate gradient method was utilized to optimize the constructed simulation box. Following optimization, these models underwent MD simulations utilizing MAPS's pre-installed LAMMPS (Large-scale Atomic Molecular Massively Parallel System) software. The MD simulations employed a modified 'Drieding' force field. The potential energy contribution from non-bonded interactions in the 'Dreiding' force field was defined by the Lennard-Jones (LJ) 12-6 potential equation [213].

$$E_{ij}^{LJ} = 4\varepsilon_0 \left[\left(\frac{\sigma_0}{r_{ij}} \right)^{12} - \left(\frac{\sigma_0}{r_{ij}} \right)^{6} \right] \qquad (6.1)$$

In Equation (6.1), ε_0 represents the potential well depth, σ_0 is van der Waals radii, and r_{ij} is the interatomic distance between atom types i and j. Table 6.2 gives the L-J parameters used in this research. Periodic boundary conditions were applied across all dimensions of the simulation cell. The temperature was maintained at room temperature (T = 298.15 K). MD simulations were conducted in the NVT ensemble over a ten-nanosecond (10 ns) period, employing a time step of one-femtosecond (1 fs). Coulomb interactions were computed using the particle mesh approach with a 12 Å cut-off distance.

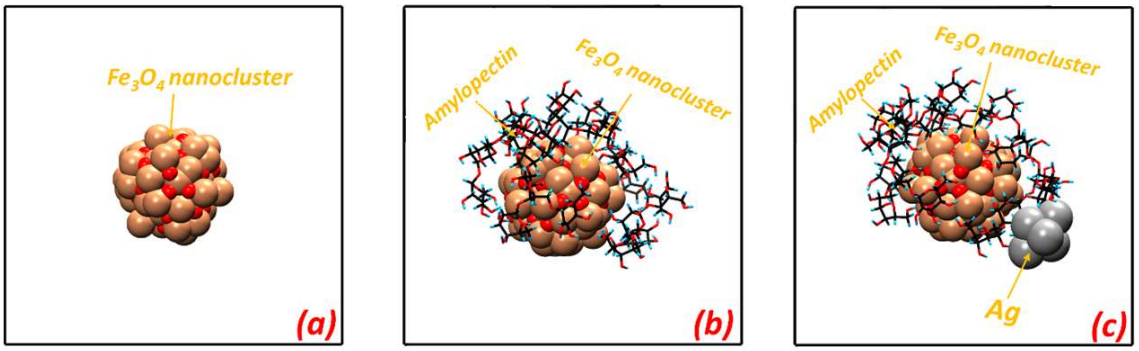

FC system **SFC system** **AgSFC system**

Figure 6.1 Snapshots of the **(a)** FC **(b)** SFC **(c)** AgSFC cluster in the center of the simulation box. The snapshots show the way initially the cluster is placed in the center of the empty simulation box.

Table 6.1. SPC water model charges.

Parameter	Value
O_W charge	-0.820
H_W charge	0.410

Table 6.2. Lennard-Jones (LJ) 12-6 potential parameters

Atom type	ε_0(Kcal/mol)	σ_0(Å)
Fe (Fe_3O_4)	0.0550	4.044680
O_3 (Fe_3O_4)	0.0957	3.033154
O_W (water)	0.1553	3.166
H_W (water)	0.0000	0.0000
C_3 (Carbon atom in amylopectin)	0.0951	3.472990
O_R (Oxygen atom in oxygen molecule)	0.0957	3.033154
H_ (Hydrogen atom attached with the carbon atom in the amylopectin)	0.0152	2.846421
Ag (silver)	0.0360	2.804549

6.3 RESULTS AND DISCUSSION

Figure 6.2 displays the XRD pattern of the as-prepared SM and ASM photocatalyst. Both diffraction patterns display peaks at scattering angles (2θ) of 18.33, 30.15, 35.51°,

37.15°, 43.2°, 53.5°6, 57.12°, and 62.70°, corresponding to the face-centered cubic Fe_3O_4 (111), (220), (311), (222) (400), (422), (511), and (440) crystal planes, respectively (JCPDS no. 88-0315). The XRD pattern of the as-prepared ASM photocatalyst also displays peaks at 2θ values of 38.12° and 44.39°, consistent with the (111) and (200) crystallographic planes of the FCC Ag (JCPDS no. 89–3722) phase, signifying the successful formation of Ag-loaded SM nanoparticles.

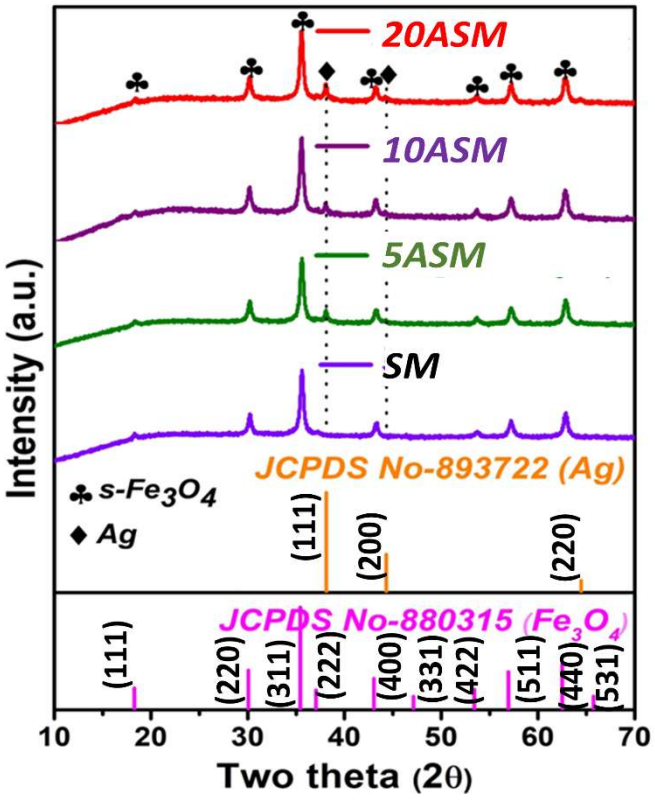

Figure 6.2. XRD patterns of pure SM and ASM photocatalysts with different percentages of Ag loaded on SM nanoparticles.

Thermo-gravimetric analysis (TGA) was conducted on pure Fe_3O_4 and SM samples to confirm the starch functionalization of Fe_3O_4 nanoparticles. The TGA was carried out at a heating rate of 5 °C min^{-1} within 40 to 500 °C in a nitrogen atmosphere. Figure 6.3 illustrates the TGA curves of the pure Fe_3O_4 and SM samples. The pure Fe_3O_4 nanoparticles displayed a weight loss of only 1.19 wt.% due to the removal of adsorbed water molecules.

In contrast, the TGA curve of the SM sample exhibited two distinct decomposition steps. The initial weight loss, occurring between 50-150°C, was ascribed to starch dehydration, while the subsequent loss, observed from around 200 °C to 500 °C, corresponded to its thermal decomposition. The starch content in SM was estimated to be 15.56% by weight.

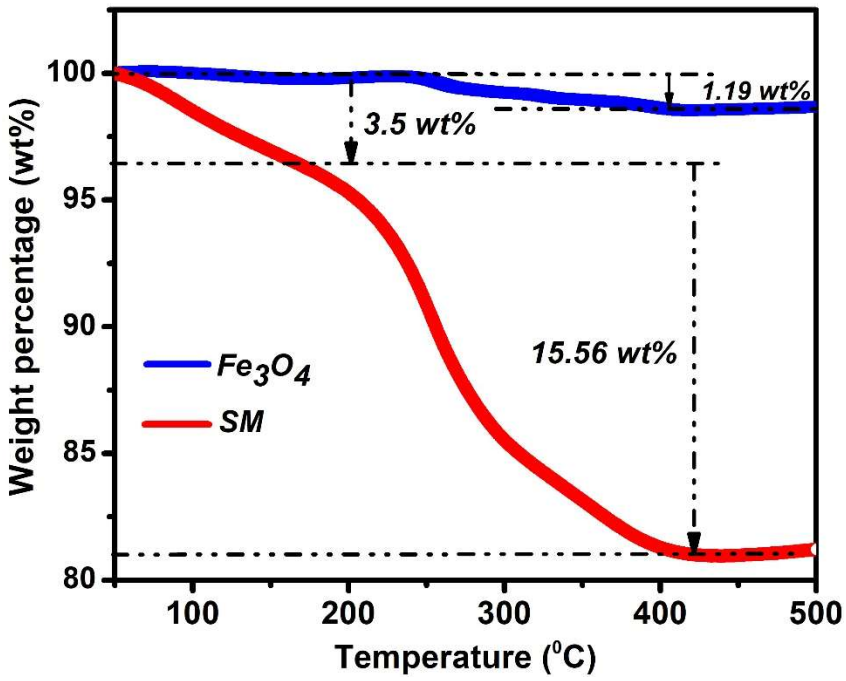

Figure 6.3 TGA analysis of Fe_3O_4 and SM samples.

Figure. 6.4 presents the TEM and HR-TEM images of pure Fe_3O_4, SM, and 10ASM nanoparticles. The TEM images reveal that pure Fe_3O_4 and SM nanoparticles are mostly spherical (Figures 6.4a and 6.4d). Figure. 6.4 (b, c) depicts the HR-TEM image and inverse fast Fourier transform (IFFT) analysis of pure Fe_3O_4. Part (c) of the figure displays lattice fringes with a d-spacing of 0.48 nm, corresponding to the (111) crystal plane of Fe_3O_4. The average particle size for pure Fe_3O_4 nanoparticles (Figure 6.4a) is approximately 25-30 nm, while SM nanoparticles (Figure 6.4d) have an average size of 10-12 nm. Thus, starch capping reduces the size of Fe_3O_4 nanoparticles. Figures 6.4e and 6.4f present the HRTEM

image and IFFT analysis of the SM photocatalyst, revealing a lattice fringe of 0.48 nm, which confirms the successful synthesis of starch-functionalized Fe_3O_4 nanoparticles.

Figure 6.4g displays the TEM image of the 10ASM photocatalyst. The HR-TEM image and IFFT analysis of 10ASM photocatalyst in Figures 6.4h and 6.4i display two adjacent regions with distinct lattice fringes 0.23 nm and 0.48 nm attributed to the (111) planes of Ag and the (111) planes of Fe_3O_4, indicating the formation of ASM nanostructures. Fig. 6.4j shows the elemental mapping of the 10ASM photocatalyst. It reveals the homogeneous distribution of Fe, O, and Ag elements in a specific region within the SEM micrograph of the 10ASM photocatalyst sample.

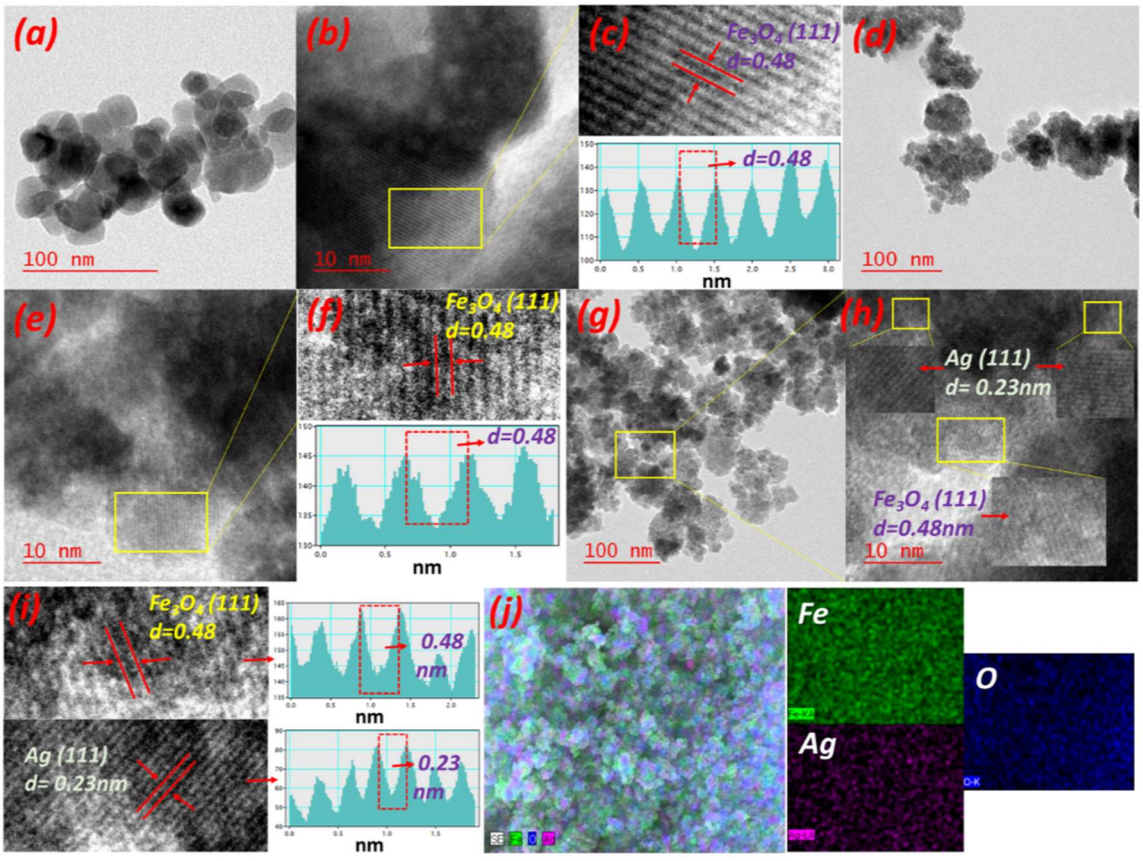

Figure 6.4. TEM, HR-TEM, and IFFT analysis of **(a–c)** pure Fe_3O_4 photocatalyst, **(d–f)** SM photocatalyst, and **(g–i)** 10ASM photocatalyst. **(j)** SEM images and corresponding elemental mapping of the 10ASM photocatalyst.

6.3.1 Optical properties

The solid-state UV-visible absorption spectra of the as-prepared photocatalysts are depicted in Figure 6.5a. It is observed that the absorption edge of the Ag-loaded SM samples falls within a similar range of visible wavelengths as the SM catalyst. The optical band gaps of Fe_3O_4, SM, and Ag-loaded SM photocatalysts were determined from the Tauc plots (derived from the Kubelka-Munk equation) [214,215].

$$(\alpha h\upsilon)^{1/n} = A\left(h\upsilon - E_g\right) \quad \text{(6.2)}$$

Here, α represents the absorption coefficient, h represents Planck's constant, υ is the light frequency, A denotes the proportionality constant, and E_g is the band-gap energy.

The Tauc plots (6.5b) reveal that the band gaps of pure Fe_3O_4, SM, and Ag-loaded Fe_3O_4 (5, 10, 20 wt.%) are 1.87, 2.28, and 2.28 eV, respectively. Moreover, it is observed that the band gap of Fe_3O_4 (1.87 eV) is enhanced after functionalization with starch due to the smaller particle size (quantum size effect) of the SM sample (2.28 eV). Figure 6.5c depicts the UV-visible absorbance spectra of aqueous sols of SM, 5ASM, 10ASM, and 20ASM nanoparticles. Compared to the SM photocatalyst, Ag nanostructures loaded on the SM surface present stronger visible light absorption. The absorption peak at 395 nm corresponds to the localized surface plasmon resonance (LSPR) absorbance of metallic Ag nanostructures on the ASM photocatalysts.

The PL spectra were acquired for SM and 10ASM using photoexcitation at 350 nm. As shown in Figure 6.5d, the PL emission intensity decreases upon incorporating silver up to 10 wt% (10ASM). The lower PL emission intensity of the 10ASM sample compared to the SM photocatalyst suggests that it has the slowest electron-hole recombination, leading to higher photocatalytic capability [216].

FTIR was employed to understand the interaction of starch and Fe_3O_4 nanoparticles. Figure 6.5e presents the FTIR spectra of Fe_3O_4 (without starch) and SM (starch functionalized) samples. In the FTIR spectrum of the SM sample, distinct peaks are observed at 2926, 1156, and 1032 cm^{-1}, matching the stretching frequencies related to C–H, glycosidic C–O–C, and C–O bonds, respectively. As anticipated, these peaks are absent from the FTIR spectrum of the Fe_3O_4 sample (before starch functionalization). The latter again confirms the successful preparation of starch-functionalized Fe_3O_4 nanoparticles. The absorption peak at approximately 3430 cm^{-1} is associated with vibrations corresponding to the stretching mode of O-H bonds. The signals at 1641 cm^{-1} and 582 cm^{-1} correspond to the hydroxyl groups on the surface of the H_2O molecule and Fe-O stretching vibrations [217,218].

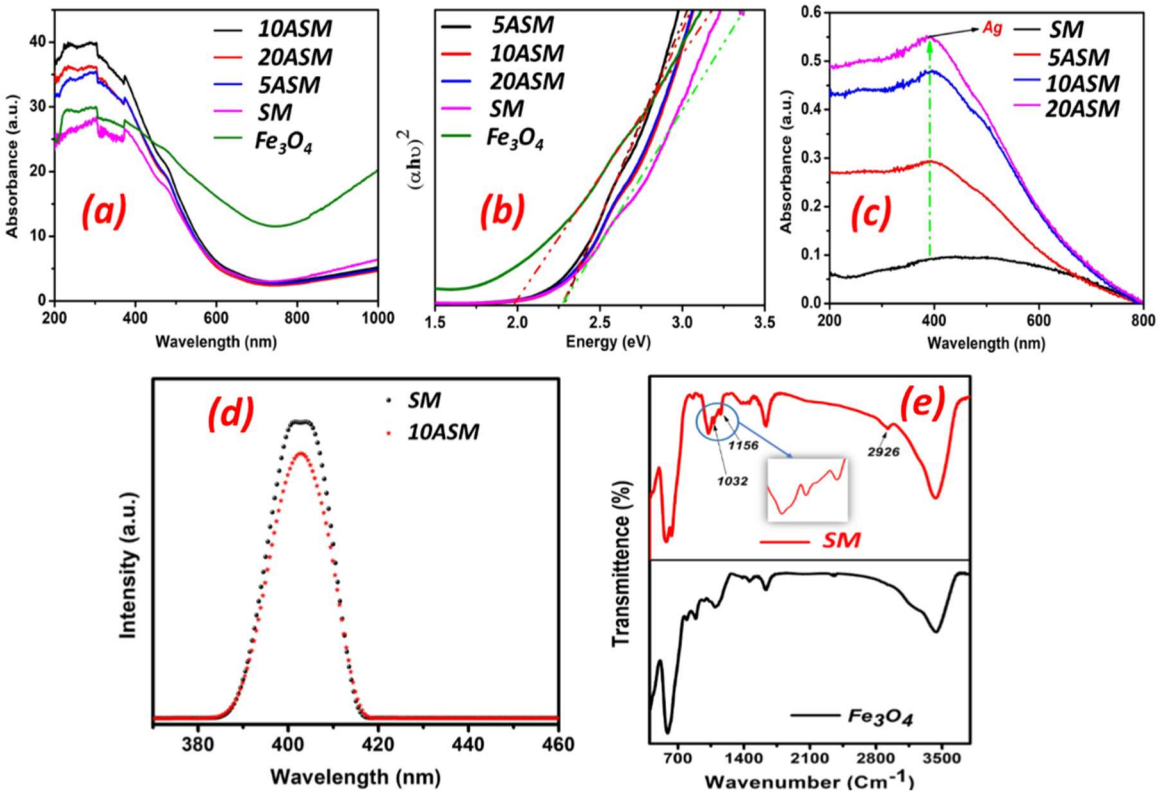

Figure 6.5. (a) The solid-state UV absorbance spectra of the as-prepared photocatalyst, **(b)** The Tauc plot, **(c)** the UV-visible absorbance spectra of aqueous sols of the nanoparticle

samples **(d)** PL spectra of SM and 10ASM photocatalysts. **(e)** FTIR spectra of Fe_3O_4 and SM samples.

6.3.2 Electrochemical Analysis

Figure 6.6a presents the electrochemical impedance spectroscopy (EIS) Nyquist plots of SM and different wt.% of Ag-loaded SM photocatalysts, while the accompanying inset depicts the corresponding equivalent circuit model used for analysis. R_{ct} and R_s represent the charge transfer and electrolyte solution resistance within the equivalent circuit model, respectively. The Ag-loaded SM samples exhibit a smaller arc radius than pure SM, showing reduced charge transfer resistance. Among all the photocatalysts, the 10ASM sample demonstrates the smallest arc radius, demonstrating lower charge transfer resistance and superior charge separation in this composite [219]. This is consistent with this sample's enhanced photocatalytic performance and lowest PL intensity observations. Figure 6.6b illustrates the visible-light-induced photocurrent responses of the SM, 10ASM samples for multiple on-off cycles. The significantly improved photocurrent density of 10ASM under light exposure provided evidence for efficient charge carrier mobility resulting from the proper interface of the metallic Ag with the SM photocatalyst. Additionally, the enhanced photocurrent density in the 10ASM composite can be attributed to the effective suppression of recombination among photogenerated charge carriers, which occurs due to the increased lifespan of excitons [219].

The Mott-Schottky (MS) plots of the samples were analyzed to determine the semiconductor type and flat band potential of the synthesized photocatalysts [220]. The plot (Figure 6.6c) exhibits a positive slope, showing that SM nanoparticles are n-type semiconductors. The x-axis intercept of the fit to the linear portion of this MS plot indicates that the CB position of SM nanoparticles is 0.28 V. The MS results are combined with the

band gap values of SM (using the equation $E_{CB} = E_{VB} – Eg$) to calculate respective VB positions [221]. Consequently, the VB positions are 2.56 V for SM. The following relationship is employed: V(NHE) = V(Ag/AgCl) + 0.059 × pH + 0.197 to convert potential measurements from the Ag/AgCl reference electrode scale to the normal hydrogen electrode (NHE) scale for all electrochemical assessments [157,222].

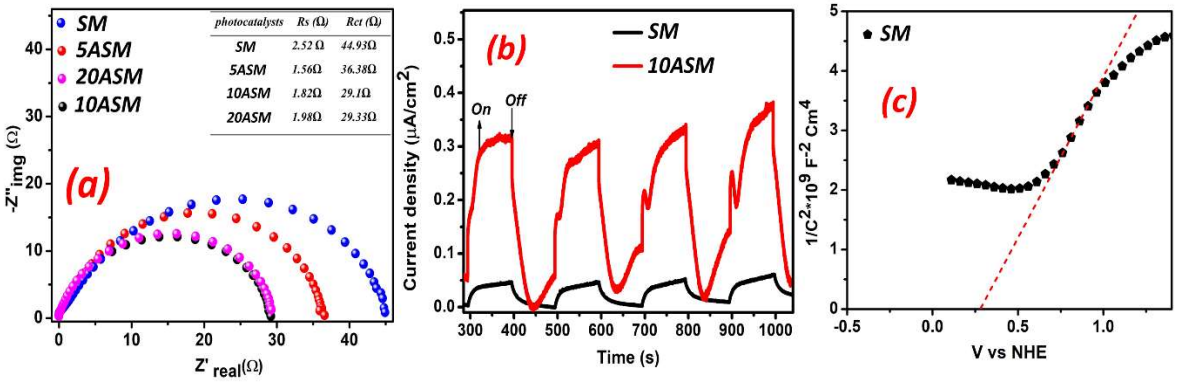

Figure 6.6 (a) Nyquist plots of pure SM and different (wt.% of) Ag-loaded SM photocatalysts, **(b)** photocurrent analysis of SM and 10ASM photocatalysts, **(c)** Mott-Schottky plot for the SM photocatalyst.

The elemental compositions and surface electronic environment of the SM and 10ASM photocatalysts were examined by XPS. Figure 6.7a demonstrates the XPS survey spectra of the SM and 10ASM samples, revealing the elemental composition of the prepared sample. This analysis confirms the presence of Fe, O, and C in SM and Fe, O, C, and Ag elements in the 10ASM samples. Figure. 6.7(b,c) compares the high resolution (HR) XPS of Fe 2p and O 1s elements in pristine SM with the same species in the 10ASM sample. Figure 6.7b shows the HR XPS of Fe 2p spectra for pristine SM and 10ASM samples. Fe $2p_{3/2}$ and Fe $2p_{1/2}$ peaks at binding energies (BE) of 709.12 eV and 722.6 eV, respectively, in the SM sample, indicating the presence of Fe^{3+} and Fe^{2+} species. Furthermore, a satellite peak at 716.8 eV and 731.6 eV also suggests the coexistence of

Fe^{2+} and Fe^{3+} (Figure. 6.7b) [223]. The Fe $2p_{3/2}$ and Fe $2p_{1/2}$ peaks show a positive shift to 710.3 and 723.8 eV in the XPS of the 10ASM sample (Figure 6.7b). The HR XPS spectra of O 1s in pure SM and 10ASM samples are shown in Figure 6.7c. The three fitted distinctive peaks of O 1s at BE of 529.3, 531, and 532.2 are attributed to the Fe-O (lattice oxygen), hydroxyl (-OH), and surface adsorbed oxygen [195,196]. These peaks shift to 529.5, 530.8, and 532.4 eV in the 10ASM sample.

The Ag 3d spectrum in Figure 6.7d displays two distinct peaks at 368.14 eV and 374.12 eV. These two peak locations correspond to the BE for Ag $3d_{3/2}$ and Ag $3d_{5/2}$, respectively, which point to the presence of metallic silver (Ag^0) [224]. Additionally, the positive BE shift in the Fe 2p and O 1s peak positions in 10ASM compared to SM photocatalyst indicates charge transfer from SM nanoparticles to metallic Ag. It also demonstrates the chemical interaction between Ag metals and SM nanoparticles at the interface of the nanostructures [120,121].

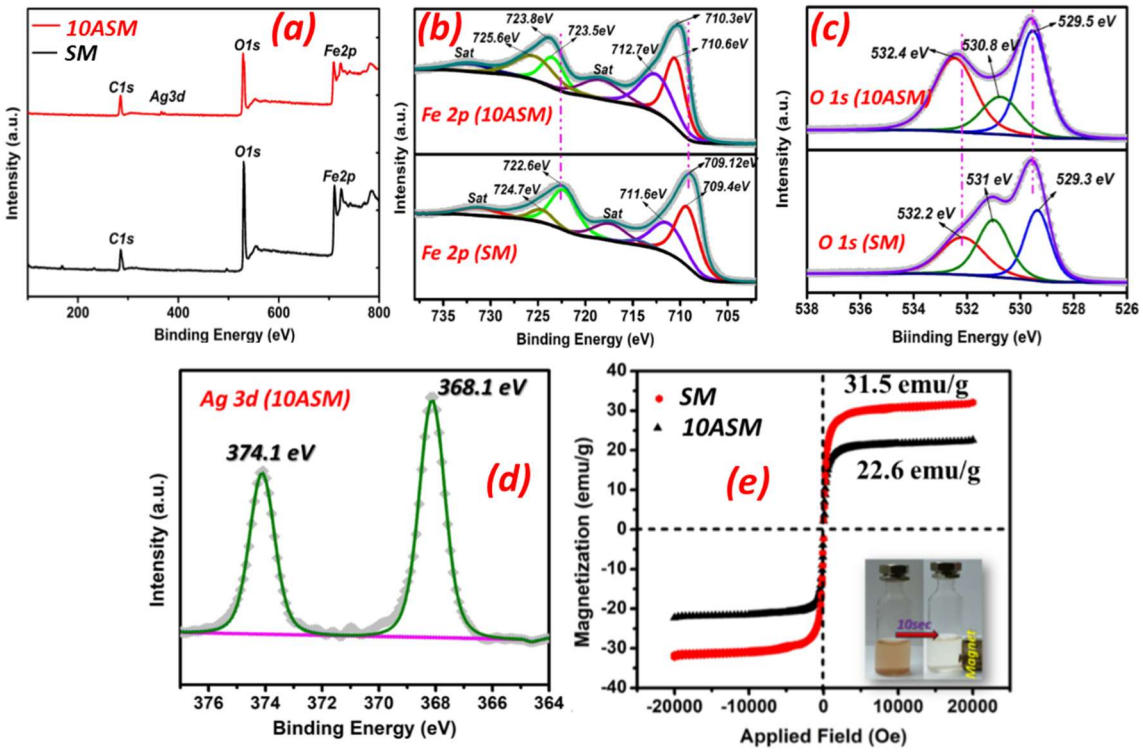

Figure 6.7 (a) XPS survey spectra of SM and ASM. HRXPS of **(a)** Fe 2p of SM and 10ASM, **(b)** O 1s of SM and 10ASM, **(c)** Ag 3d of 10ASM photocatalyst. **(d)** Magnetization versus applied magnetic field plots of SM and 10ASM photocatalysts. The inset picture is of an aqueous dispersion of photocatalyst nanoparticles before and after magnetic separation.

Figure. 6.7e shows the magnetization versus magnetic field (M-H) curves of SM and 10ASM photocatalyst in the -20 kOe $< H <$ $+20$ kOe range at room temperature (300K). The photocatalysts SM and 10ASM demonstrated saturation magnetization (Ms) values of 31.5 and 22.6 emu/g, respectively. The S-shaped M-H curve with negligible hysteresis showed that the prepared nanoparticle samples were superparamagnetic [225,226]. These magnetic properties facilitate efficient magnetic separation of the photocatalyst when subjected to an external magnetic field. The inset image in the figure shows that the photocatalyst nanoparticles can be separated within 10 seconds using an external magnetic field.

6.3.3 MD results

Figure 6.8 (a-c) depicts the FC, SFC, and AgSFC system's snapshot at the end of a 10 ns equilibration run. The figures illustrate the distribution of O_2 and H_2O molecules surrounding Fe_3O_4, SM, and ASM units. However, this depiction lacks quantitative insight into the probability of O_2 and H_2O positions relative to the photocatalysts Fe_3O_4, SM, and ASM clusters. The snapshot of the ASM model in Fig. 6.8c clearly shows the adsorption of O_2 molecules on the Ag nanocluster (denoted by the green circle).

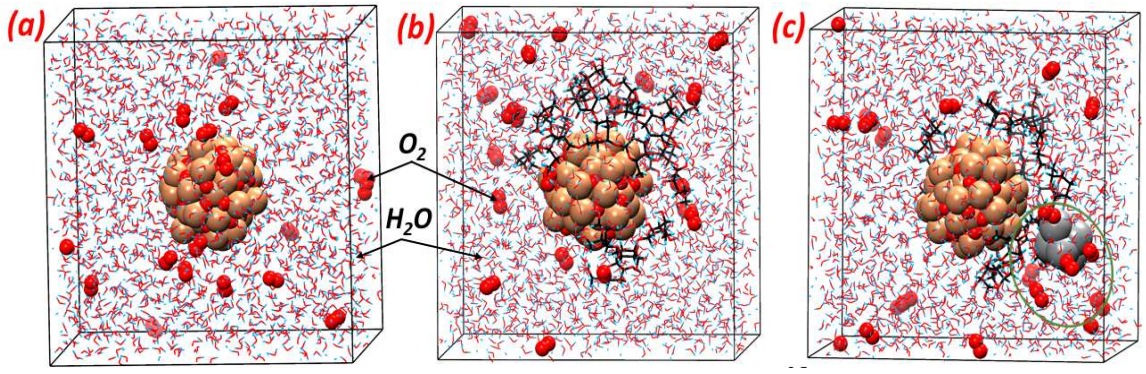

Figure 6.8. (a) shows the snapshot of the simulated system. **(a)** FC model **(b)** SFC model **(c)** AgSFC**.**

The intermolecular Radial Distribution Function (RDF) plots depicted in Figure 6.9 elucidate the nature of interactions between different atom types comprising the FC, SFC, and AgSFC systems. RDF gives the atom type to atom type most probable distance. Contrary to this, CM-RDF plots give a molecule's probable distance from the nanocluster's center in the modeled system. The RDF plots probe the molecular associations between iron (Fe) and oxygen (O) atoms in the Fe_3O_4 nanocluster with atom types making O_2 and H_2O molecules. Table 6.3 provides a comprehensive table detailing the atom-type nomenclature across all figures (Table 6.3). The first interaction peak emerges at approximately 2.6 Å in the RDF of the FC. It demonstrates significant interaction between Fe atoms of Fe_3O_4 and O atoms of O_2 molecules. Another peak in Figure 6.9a, which occurs at 2.9 Å, is between the Fe atoms of Fe_3O_4 and O atoms of H_2O molecules.

Figure 6.9b shows the SFC (RDF) plots between atom types in SM and those in O_2 and H_2O molecules. Notably, amylopectin (AMC) molecules are partially adsorbed onto the Fe_3O_4 nanocluster, leading to intermolecular interactions between AMC atom types (e.g., C and H) and the O atoms of both O_2 and H_2O molecules. The H_HB atoms of AMC in the SM system display strong interaction peaks around 1.7 Å and 2.07 Å due to interactions between H_HB--O_W and H_HB--O_R. Similarly, two other peaks of H_

atoms of AMC in the SM system show interactions between H_--O_R and H_--O_W at approximately 2.3 Å. The C_3 atoms of AMC in the SM system also show interactions with O_W and O_R at a similar peak distance of 3 Å. The Fe atoms of the SM system display notable peak intensities for Fe--O_W and Fe--O_R at 1.56 Å and 2.9 Å, respectively.

Prominent peaks in the AgSFC systems (Figure 6.9c) demonstrate Ag has a strong interaction with the O_R atom type in the 2.5 to 3 Å range. The Ag atom type also interacts with the O_W atom type at a similar distance. At the same distance, there is also a strong interaction between the amylopectin H_HB and the O_W atom types. Thus, functionalizing Fe_3O_4 with starch (SM system) enhances water adsorption affinity, and incorporating Ag onto SM (ASM) increases O_2 adsorption affinity.

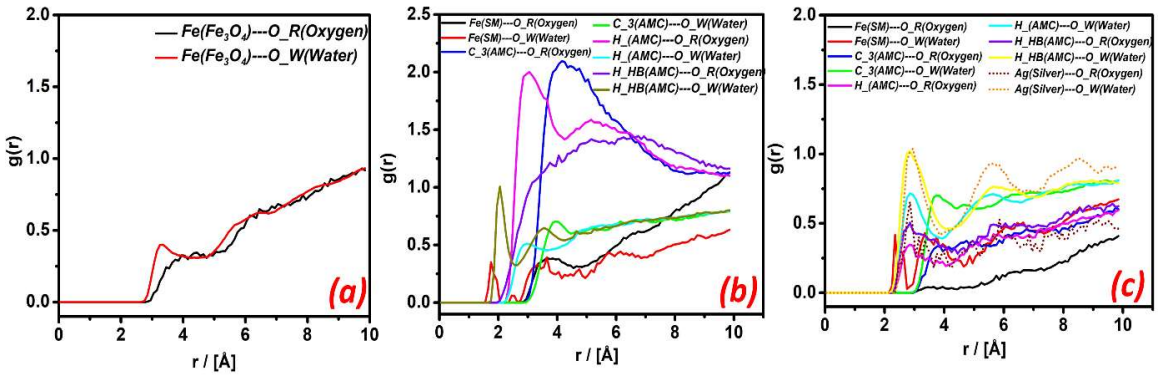

Figure 6.9. RDF (g(r)) vs distance of interaction r/[Å] **(a)** Fe_3O_4 model **(b)** SM **(c)** ASM model.

Table 6.3. The naming convention is followed in the RDF plots.

Atom type	Meaning
Fe	Iron atom in Fe_3O_4
O_R	Oxygen atom in O_2 molecule
O_W	Oxygen atom in the H_2O molecule

Ag	Silver atom of Ag cluster
H_HB	Hydrogen atom attached to an oxygen atom in the amylopectin
H_	Hydrogen atom attached with the carbon atom in the amylopectin
C_3	Carbon atom in amylopectin

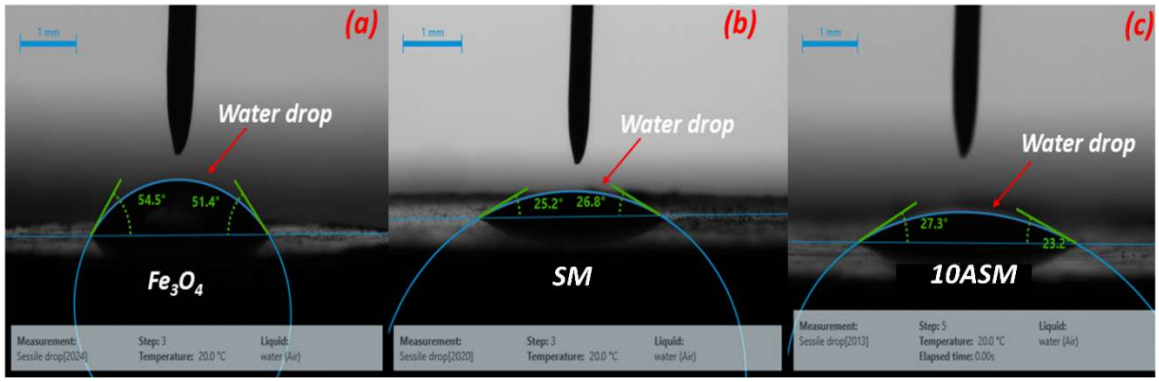

Figure 6.10. Contact angle measurement on **(a)** Fe_3O_4, **(b)** SM, and **(c)** 10ASM photocatalysts.

6.3.4 Photocatalytic H_2O_2 production activity

No H_2O_2 production was detected on the prepared photocatalysts under dark conditions. Subsequently, all samples' photocatalytic activities for H_2O_2 production were evaluated under visible light irradiation using only water at neutral pH. The pristine Fe_3O_4 and SM (without silver loading) nanoparticles showed inefficient H_2O_2 production due to poor visible light absorption and quick photoinduced charge carrier recombination. Compared to this, a considerable amount of H_2O_2 formation was detected from pure water following 60 minutes of visible light exposure at a neutral pH (~6.9) on Ag-loaded SM nanostructures. The H_2O_2 production on 10ASM was calculated to be 167 $\mu molg^{-1}h^{-1}$ and ~16 times higher than that of SM. The 10 wt% Ag loading on the SM nanostructure photocatalyst exhibits optimal photocatalytic H_2O_2 production activity at 60 min light

exposure because it facilitates efficient interfacial charge transfer and enhanced charge separation. In contrast, increasing the Ag loading to 20 wt.% leads to agglomeration and excessive surface coverage. This can block active sites, reduce light penetration, and create recombination centers, ultimately lowering the photocatalytic activity. Figure 6.11a indicates that the 10AM photocatalyst, without starch functionalization, also exhibited an H_2O_2 generation rate of 83 μmol/g/h. This value is almost half the H_2O_2 generation rate observed for the 10ASM (starch functionalized) photocatalyst. This comparison suggests that the starch-functionalized Ag-loaded Fe_3O_4 (10ASM) photocatalyst significantly enhances its photocatalytic activity for H_2O_2 production. Starch functionalization on Fe_3O_4 makes its surface considerably more hydrophilic, demonstrating strong water adsorption. The increase in photocatalyst surface hydrophilicity likely improves the water oxidation efficiency, resulting in a higher H_2O_2 generation rate.

To explore the surface properties of the synthesized Fe_3O_4, SM, and 10ASM photocatalysts, the water contact angle (WCA) was measured on a pellet of each photocatalyst (Figure 6.10). A decrease in the WCA indicates strong material adsorption (hydrophilicity). Pure Fe_3O_4 (without starch) displays a contact angle of 52.95°, highlighting its poor water adsorption (hydrophobic) nature (Figure 6.10a). Following the functionalization with starch and Ag loading on Fe_3O_4, the resulting photocatalysts, SM and 10ASM, exhibit calculated contact angles of 26° and 25.2°, respectively, indicating an enhancement in hydrophilic properties (Figure 6.10b, c). These findings demonstrate that the improved hydrophilicity of 10ASM promotes more efficient water oxidation. This also leads to longer residence times for solvent molecules, improving their interaction with photocatalyst particles and reactants [127].

The photocatalytic experiments were conducted under four different pH conditions (pH 2, 3, 5, and 7) to investigate the influence of pH on H_2O_2 generation. The results

revealed that the photocatalytic H_2O_2 production was significantly affected by the pH of the aqueous solution. Figure 6.11b shows that 10ASM exhibited the highest photocatalytic activity for H_2O_2 production at pH 3 (258.7 μmol/g/h) compared to the other three pH values. This observation suggests that excess protons at pH 2 might gradually oxidize the produced H_2O_2 into H_2O ($H_2O_2 + 2H^+ + 2e^- = 2H_2O$). Conversely, in a less proton-rich environment at pH 5 and 7, the H_2O_2 production was lower due to faster H_2O_2 decomposition [227]. Consequently, a pH value of 3 was optimal for photocatalytic H_2O_2 production.

To gain more insight, additional controlled experiments were conducted to investigate how different gas environments (Air, O_2, and N_2) affect the photocatalytic activity of the 10ASM photocatalyst in H_2O_2 production (Figure 6.11c). The findings indicate that substituting O_2 with N_2 leads to a notable inhibition of the photocatalytic efficiency in the oxygen reduction reaction (ORR), emphasizing the crucial role of dissolved O_2 during the ORR to H_2O_2 production process. To compare the results, photocatalytic tests were also conducted with different sacrificial agents (ethanol, IPA, and glycerol) on the 10ASM photocatalyst to determine whether these electron donor molecules could speed up the formation of H_2O_2. Adding 5-vol% % glycerol in water enhances (~2.5 times) the formation of H_2O_2 compared to pure water at pH 3. Figure 6.11d compares the photocatalytic H_2O_2 formation activity on a 10ASM sample with different sacrificial agents after 60 minutes of visible light irradiation. Additionally, Figure 6.11h compares the results of photocatalytic H_2O_2 production of 10ASM with other reported photocatalysts under different sacrificial agents in recent years. Detailed information on the previously reported photocatalysts is mentioned in Table 6.4.

The photocatalytic H_2O_2 formation experiment was repeated five times to examine the recyclability of the 10ASM catalyst further. After each cycle, the photocatalyst was

washed with distilled water, then isolated from the solution using an external magnetic field, and the recovered sample was used for the subsequent reaction. The recyclability results show that the photocatalytic H_2O_2 production remained almost unaltered for subsequent runs, as shown in Figure 6.11e. Additionally, to investigate the sample stability of the 10ASM, the XRD pattern of the photocatalyst was recorded after the fifth cycle. No change in the recycled sample XRD pattern was observed, indicating the stability of the photocatalyst for H_2O_2 production (Figure 6.11f). Hence, the 10ASM photocatalyst demonstrated excellent photostability for efficient H_2O_2 generation photocatalysis.

Additionally, the influence of catalyst amount on photocatalytic H_2O_2 production was evaluated using 1 mg, 2 mg, and 4 mg of the 10ASM photocatalyst in a 12 mL reaction volume (Figure 6.11g). The H_2O_2 yield increased from 630.7 μmol g^{-1} h^{-1} at 1 mg to a maximum of 651 μmol g^{-1} h^{-1} at 2 mg, owing to the greater number of active sites and enhanced light harvesting. However, further increasing the loading to 4 mg led to a slight decrease in yield (622 μmol g^{-1} h^{-1}). This reduction can be attributed to light scattering and shielding effects at higher solid concentrations, which limit photon penetration and may also promote charge carrier recombination due to interparticle interactions.

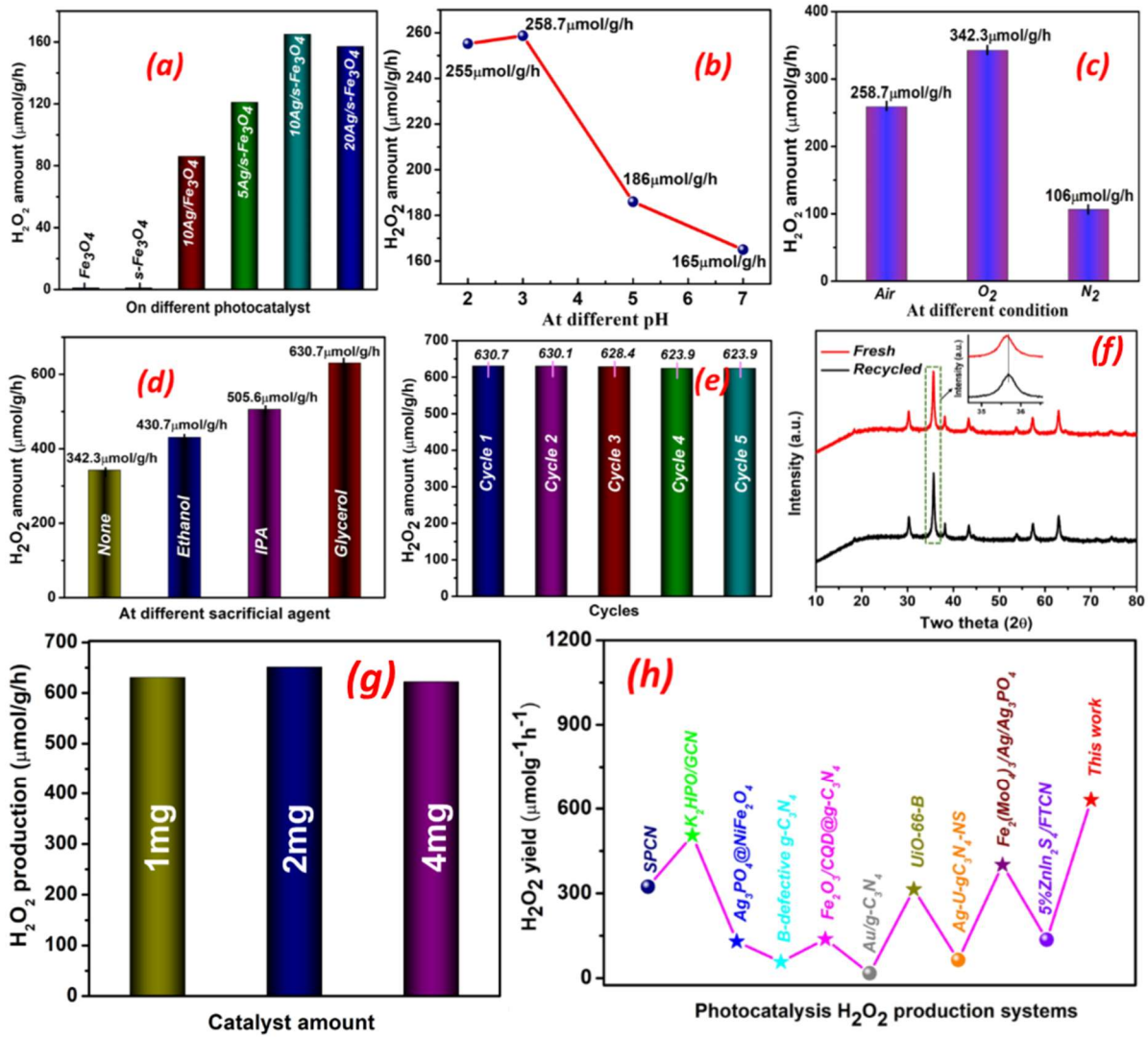

Figure 6.11 (a) H_2O_2 production on different samples from pure water at neutral pH **(b)** H_2O_2 production at different pH on 10ASM photocatalyst **(c)** H_2O_2 production at different conditions on 10ASM photocatalyst **(d)** H_2O_2 production using different sacrificial agents on 10ASM photocatalyst **(e)** Recyclability performance of 10ASM photocatalyst in aqueous solution of glycerol **(f)** XRD of recycled photocatalyst (10ASM) **(g)** Effect of catalyst amount on photocatalytic H_2O_2 production on 10ASM photocatalyst **(h)** comparison data for photocatalytic H_2O_2 production with other previously reported photocatalysts in recent works.

Table 6.4 Comparison of photocatalytic H_2O_2 production with other previously reported photocatalysts from different sacrificial agents in recent works.

Photocatalysts	Reaction condition	Catalyst dosage (g/L)	H_2O_2 production ($\mu molg^{-1}h^{-1}$)	Ref
SPCN	10%IPA containing DW; Visible light ($\lambda > 420$ nm)	0.5	323.6	[228]
K_2HPO/GCN	10% EtOH containing DW mixture; Visible light ($\lambda > 420$ nm)	1	505	[229]
Ag_3PO_4@$NiFe_2O_4$	75 vol% MeOH/ O_2 saturated DW; 300W Xe lamp ($\lambda > 420$ nm)	0.2	130	[64]
B-defected g-C_3N_4	10 vol% IPA containing water; $\lambda \geq 420$ nm	0.5	57.4	[230]
Fe_2O_3/CQD@g-C_3N_4	10% EtOH / O_2 saturated DW mixture; 300W Xe lamp ($\lambda > 420$ nm)	0.5	138.6	[231]
Au/g-C_3N_4	(1/9v/v) EtOH/O_2 saturated water mixture; $\lambda \geq 420$ nm	4	16.89	[232]
BN QDs/Ultrathin porous g-C_3N_4	(1/9v/v) IPA/O_2 saturated water mixture; $\lambda \geq 420$ nm	1	72.3	[233]
UiO-66-B	(1/9v/v) IPA/O_2 saturated water mixture; AM 1.5	0.3	314	[234]
Au@U-g-C_3N_4	1/9v/v) EtOH/O_2 saturated water mixture; 300W Xe lamp	1	64.29	[142]
$Fe_2(MoO_4)_3$/Ag/Ag_3PO_4	Methanol/water mixture; UV-visible light	0.2	400.8	[141]
5%$ZnIn_2S_4$/FTCN	10% EtOH / O_2 saturated DW mixture; Visible light ($\lambda > 420$ nm)	0.5	135.98	[67]

10ASM	5 vol% glycerol/ O_2 saturated DW; Cool day white LED (1070w/m^2)	0.083	630.7	This work

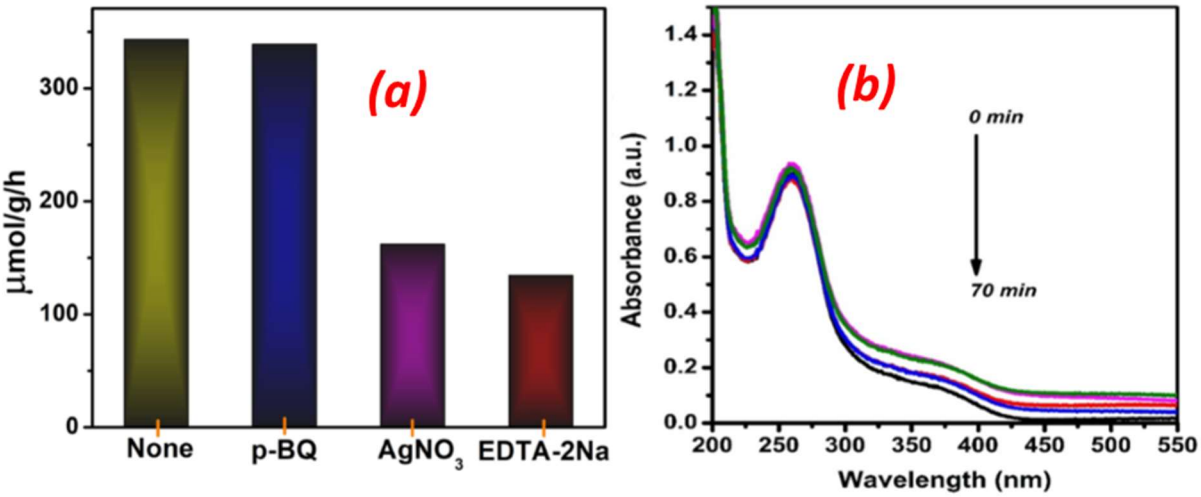

Figure 6.12. (a) Effect of different trapping agents on photocatalytic H_2O_2 production on 10ASM photocatalyst **(b)** NBT test on 10ASM.

6.4 Photocatalytic H_2O_2 production mechanism

The schematic in Figure 6.13 proposes a possible photocatalytic H_2O_2 formation on the ASM photocatalyst. The series of experiments and MD simulation results facilitated the development of this mechanism. The experimental results show that photocatalytic H_2O_2 production activity increases substantially on the 10ASM photocatalyst compared to pristine and different Ag-loaded SM. The EIS, PL, and photocurrent results indicate that charge separation on the 10ASM photocatalyst reduces the likelihood of charge carrier recombination.

Active species trapping experiments were conducted using p-benzoquinone (PBQ), $AgNO_3$, and ethylenediamine tetraacetic acid disodium (EDTA-2Na) as scavengers for superoxide radicals ($\cdot O_2^-$), electrons (e^-), and, hole scavenger, respectively. As shown in

Figure 6.12a, there is a significant decrease in H_2O_2 yield when $AgNO_3$ and EDTA-2Na are employed as scavenger agent, which means that electrons (e^-) and holes (h^+) play a crucial role in the oxygen reduction and water oxidation reaction. The performance of H_2O_2 production remains unaffected by the addition of PBQ, indicating superoxide radicals are not the active species for photocatalytic H_2O_2 generation. The formation of the $\cdot O_2^-$ in the photocatalytic reaction is further examined by the nitro blue tetrazolium test (NBT). Figure 6.12b depicts the absorption peak intensity of the NBT solution at 262 nm. Following the photocatalytic reaction, no alterations were noted in the absorption peak of the NBT solution, confirming that $\cdot O_2^-$ does not serve as an active species in reducing O_2 to produce H_2O_2.

The photocatalytic activity is directly affected by the effective adsorption of reactants, particularly water and oxygen. Therefore, it is vital to consider H_2O and O_2 adsorption on the photocatalyst surface in aqueous conditions. As illustrated by the MD simulation results, water adsorption predominantly takes place on the SM surface, and oxygen adsorption takes place on the Ag of the ASM nanostructure. Starch functionalization of the Fe_3O_4 improves its hydrophilicity, which is necessary for efficient water oxidation. WCA measurements show that the 10ASM photocatalytic system has maximum water adsorption affinity.

The visible light illumination of the ASM photocatalyst photo-excited electrons from VB of the SM component. The H_2O molecules were oxidized on photo-generated holes in the VB of the photocatalyst, generating the H^+ and O_2. Note that the VB position of SM is 2.56 V vs. NHE, providing sufficient overpotential for water oxidation (1.23 eV vs. NHE). H_2O_2 concentrations of 258.7 μmol/g/h and 106 μmol/g/h were maintained without an external O_2 supply. This observation indicates that O_2 is generated through water oxidation. Moreover, adding a suitable sacrificial agent (such as ethanol, IPA, or glycerol)

significantly boosts H_2O_2 production by promoting its activation. This enhancement occurs as photogenerated holes are effectively scavenged through the oxidation of the sacrificial agent. Additionally, this process generates H^+ ions, which subsequently react with adsorbed O_2 via the $2e^-$ ORR to produce H_2O_2 ($O_2 + 2H^+ + 2e^- \rightarrow H_2O_2$).

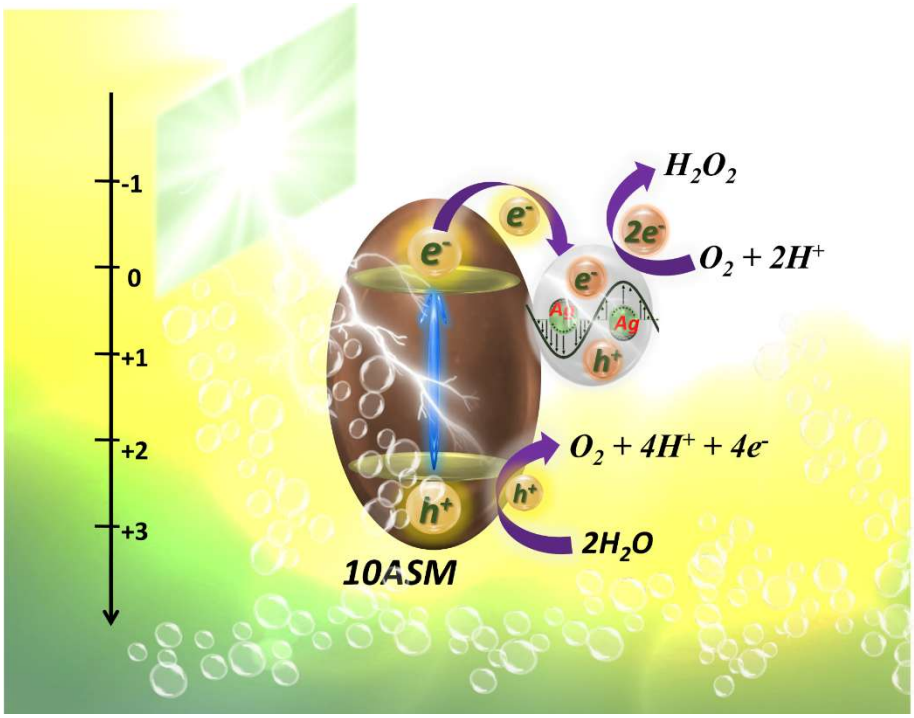

Figure 6.13 Proposed mechanism for photocatalytic H_2O_2 production on 10ASM.

6.5 Conclusions

An efficient, visible-light-driven, and magnetically recyclable photocatalyst (ASM) for H_2O_2 production was successfully synthesized using a two-step precipitation method. Fine Ag nanostructures were deposited on starch-functionalized Fe_3O_4 nanoparticle surfaces, where starch functionalization played a crucial role in preventing nanoparticle aggregation and reducing their size. Furthermore, water contact angle (WCA) measurements confirmed that starch functionalization enhances water wettability, making the photocatalyst surface more hydrophilic. MD simulations revealed that Ag loading on SM enhances O_2 adsorption, while starch improves water molecule adsorption. The

increased O_2 adsorption on Ag nanostructures is well known for facilitating oxygen reduction via the two-electron pathway, leading to efficient H_2O_2 production. Additionally, scavenger experiments confirmed that photocatalytic H_2O_2 production over ASM occurs through the two-electron O_2 reduction pathway. The Ag loading on SM was optimized, with 10 wt.% Ag deposition exhibiting the highest photocatalytic H_2O_2 production activity. However, excessive Ag deposition (20 wt.%) reduced photocatalytic performance by covering the active sites on the SM surface, while 5 wt.% Ag loading resulted in poor charge transfer efficiency. The combined experimental and molecular dynamics study provides valuable insights for designing efficient photocatalysts for H_2O_2 production via the two-electron O_2 reduction pathway. This investigation highlights the significance of concurrent water adsorption on the VB part and oxygen interaction with the CB part of the photocatalyst for designing effective H_2O_2-producing photocatalysts.